

Frontiers

Three-dimensional imaging of earth and planetary materials

William D. Carlson *

Department of Geological Sciences, University of Texas at Austin, Austin, TX 78712, United States

Received 26 August 2005; received in revised form 18 May 2006; accepted 9 June 2006

Available online 23 August 2006

Editor: A.N. Halliday

Abstract

X-ray computed tomography, neutron computed tomography, and magnetic resonance imaging are driving novel scientific advances by enabling rapid, non-destructive, three-dimensional examination and analysis of earth and planetary materials. Discoveries catalyzed by these approaches range across fields from environmental geology to petroleum geology, hydrology to soil science, paleontology to petrology, and geodynamics to meteoritics. They have impacted our understanding of hydrocarbon reservoirs, contaminant transport, climate change, CO₂ sequestration, the evolution of life, crustal uplift, mantle metasomatism, planetary differentiation, and more. Three-dimensional imaging is likely soon to become an essential component of every investigator's toolkit, especially as instruments and facilities emerge that are optimized for increasingly sophisticated geological applications of these techniques, and as access to them expands.

© 2006 Elsevier B.V. All rights reserved.

Keywords: X-ray computed tomography; neutron computed tomography; magnetic resonance imaging; visualization

1. Introduction

Because the earth and planetary sciences are founded on direct observation of natural systems, breakthroughs in understanding often come from technological advances that produce novel ways to inspect, characterize, and analyze natural materials. Technologies that generate three-dimensional (3D) imagery of geological materials — in particular X-ray computed tomography (XCT), neutron computed tomography (NCT), and magnetic resonance imaging (MRI) — are now stimulating new discovery and answering old questions. These techniques allow visualization and measurement of features in the interior of optically opaque macroscopic objects, rapidly and non-destructively. This

article offers an introduction to each of them, and provides a view of the state-of-the-art in the application of each to problems in the earth and planetary sciences, by sampling recent examples in the literature.

2. Overview of 3D imaging techniques

XCT, NCT and MRI are complementary techniques. Each interrogates the specimen by fundamentally different means, and each is therefore sensitive to different aspects of the specimen's physical and chemical configuration.

XCT and NCT measure the attenuation (reduction in intensity) of an incident beam as it passes through the sample along a number of different paths. XCT illuminates the specimen with X-ray photons, which interact principally with electrons in the target, so contrast in XCT images is generated by local differences

* Tel.: +1 512 471 4770; fax: +1 512 471 9425.

E-mail address: wcarlson@mail.utexas.edu.

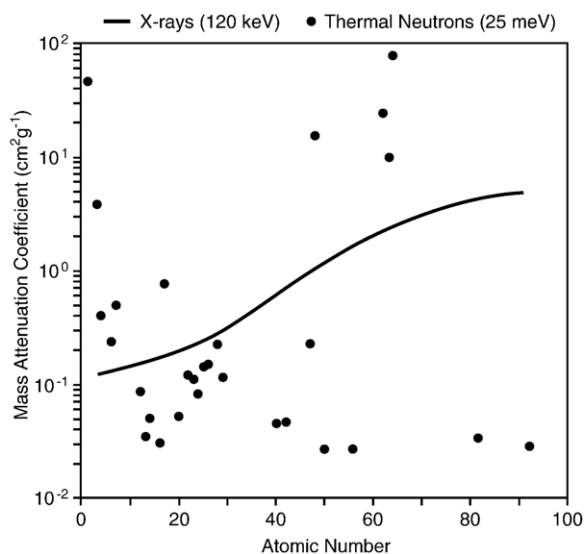


Fig. 1. Dependence of mass attenuation coefficients on atomic number for 120 keV X-rays (line) and 25 meV thermal neutrons (dots).

in mass density and mean atomic number. NCT probes the specimen with a beam of neutrons, which interact principally with atomic nuclei in the target, so contrast in NCT images is generated by local differences in the cross-sections for neutron absorption and scattering, and thus reflects elemental (and to some degree isotopic) composition. MRI is a spectrometric technique, thus distinctly different from XCT and NCT. It immerses the specimen in pulsed magnetic-field gradients, which yields information on local differences in the abundance of particular nuclei with unpaired nuclear spins.

The range of earth and planetary science applications for each of these techniques is largely governed by the specimen characteristics to which they are most sensitive. The versatility of XCT stems from its sensitivity to material properties (density, composition) that commonly show variation in diverse types of geological specimens. NCT, by contrast, is particularly sensitive to the presence of several elements that contribute little to X-ray attenuation. Fig. 1 illustrates the contrasting dependence of *mass attenuation coefficients*¹ on atomic number for X-rays and for neutrons. Whereas X-ray attenuation escalates smoothly and monotonically with atomic number, neutron attenuation shows variations that are less systematic. Of the elements common in rock-forming minerals, hydrogen has by far the highest mass attenuation coefficient, so NCT is particularly well-suited to imaging hydrous minerals and hydrogen-bearing fluids. The MRI

response in most geological imaging is strongly dominated by ¹H in liquid and mobile phases, and this sensitivity renders MRI ideal for studies involving aqueous liquids and gases, as well as nonaqueous-phase liquids (NAPLs; e.g., gasoline, solvents, coal tar).

All three techniques generate 3D datasets in which the specimen is represented by an array of volume elements or *voxels*, each of which is assigned a grayscale that correlates with the value at that position of the material property being measured. In both XCT and NCT, measurements of beam transmissivity along different linear paths through the specimen are combined via a mathematical inversion process called *reconstruction* to yield determinations of *linear*

Table 1
Glossary of specialized terminology

<i>Beam-hardening</i>	In XCT, the shift to higher values of the mean energy of a polychromatic X-ray beam, caused by greater attenuation of its lower-energy components during passage through the specimen.
<i>Compton scattering</i>	In XCT, an interaction of the electron beam with the specimen in which the X-ray photon diverges in direction from the incident beam while losing a portion of its energy to the specimen by liberating an electron from it.
<i>Linear attenuation coefficient</i>	In XCT and NCT, the local capacity of the specimen to reduce the intensity of the X-ray or neutron beam by any combination of processes of absorption and scattering, measured per unit length of the beam path.
<i>Mass attenuation coefficient</i>	In XCT and NCT, the local capacity of the specimen to reduce the intensity of the X-ray or neutron beam by any combination of processes of absorption and scattering, measured per unit mass in the beam path.
<i>Nuclear spin density</i>	In MRI, the local abundance of nuclei with resonating spins (intrinsic angular momenta) contributing to the strength of the MRI signal from a region.
<i>Photoelectric absorption</i>	In XCT, an interaction of the X-ray beam with the specimen that results in complete absorption of an X-ray photon by the specimen and emission of an electron from it.
<i>Reconstruction</i>	A general term for the mathematical process by which the measured XCT, NCT, or MRI signal is converted to a 2D or 3D image. Various procedures are employed (e.g., “filtered back-projection”, the “Feldkamp algorithm”, or Fourier-transform methods) depending on the technique, and on the particular implementation or instrument used.
<i>Sequence</i>	In MRI, the specific progression of RF pulses, and applied magnetic fields and gradients, used to excite and modulate nuclear spin transitions in the specimen, and to measure its MR response.
<i>Voxel</i>	In a 3D dataset, the minimum volume element; analogous to a 2D picture element or “pixel”.

¹ Italicized terms in the text appear in the glossary of Table 1.

attenuation coefficients at each point in the sample. The brightness of each voxel in a 3D image varies with the linear attenuation coefficient in that region. MRI, on the other hand, infuses positional information into the resonance signal by spatially selective excitation of spins in a magnetic-field gradient. Reconstruction is typically accomplished via a Fourier-transform method that extracts the intensity of the NMR signal originating in each voxel, which depends on the nuclear spin density there, but also upon numerous physical and experimental factors. The brightness of each voxel varies in proportion to the NMR signal intensity.

Interpretation of these datasets commonly requires a combination of data enhancement, visualization, and quantitative image-analysis in 3D. Several commercially available software packages offer 3D data-enhancement capabilities such as noise reduction, edge sharpening, etc., along with the ability to view arbitrarily oriented sections through the 3D volume, and to create 3D representations of objects or surfaces by isocontouring or volume rendering. Isocontouring defines the boundaries of objects in the dataset on the basis of their grayscale values, computes the position of each object's surface, then renders and displays a perspective view of that surface. Volume rendering allows the user to assign to each voxel in the data set a red–green–blue (or grayscale) value and a level of transparency/opacity, permitting visual accentuation of features of interest by rendering their surroundings transparent or nearly so. Visualizations in 3D commonly benefit from animations that present a progression of views of the dataset, and from interactive software that allows the user to choose an arbitrary viewing angle and position; these enhancements reveal the full dimensionality of the objects in the imagery. More difficult than visualization is extraction from the dataset of reliable quantitative measures of features of interest. Inherent limitations on spatial resolution, combined with the variety of artifacts that can arise in each of these imaging techniques, may introduce considerable complexity into efforts to extract highly precise and accurate quantitative information from the imagery. Commercial products to aid object quantification in 3D have begun to appear, but optimal results will likely require specialized software that incorporates tools to deal with the complexities specific to each imaging technique: an excellent example has recently appeared in the field of XCT [1].

3. X-ray computed tomography

Soon after the use of medical CAT scanners for clinical diagnosis became widespread in the 1980s, medical machines and protocols were adapted to address 3D X-

ray imaging problems in engineering and materials science, and in the earth and planetary sciences as well. Applications in these fields drove rapid evolution of specialized industrial XCT technology, unhindered by the limitations on X-ray energy, maximum dosage, and imaging time that governed design of medical instruments. The result was development of a diverse array of non-medical devices, optimized for analysis of denser objects and capable of far greater penetration, or much higher spatial resolution, or both. XCT systems suitable for geological applications now span a range of technologies that employ a variety of X-ray sources/detectors and geometrical configurations. These systems are differentiated principally by the size of the specimens each is best suited to scan, and thus by the spatial resolution that each achieves. All of these systems, however, are based on a common set of technical principles, outlined below. For readers seeking more in-depth information, synoptic summaries of the XCT technique (e.g., [2,3]) serve as useful introductions to more complete technical treatments (e.g., [4,5]).

3.1. Technical principles

All XCT systems are designed to illuminate an object with X-rays traveling along multiple intersecting paths,

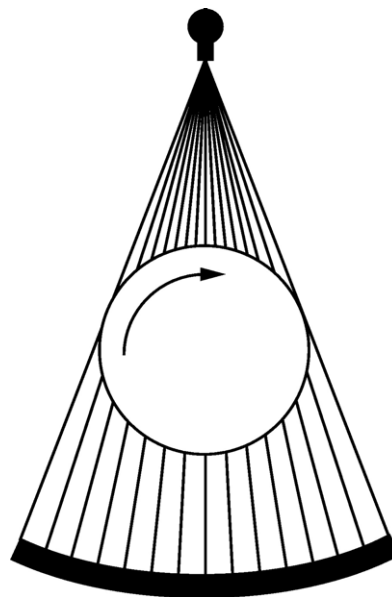
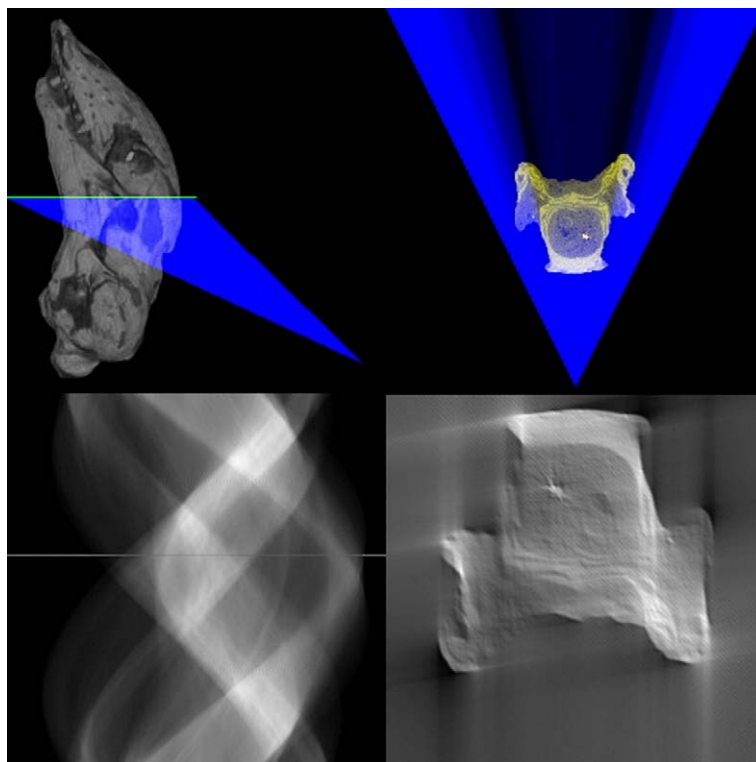


Fig. 2. Schematic illustration of one configuration commonly used for acquisition of XCT data. Arrow indicates rotation of object during data collection; solid lines passing from source (*top*) to detector array (*bottom*) are ray paths. Collection of multiple views as object rotates allows calculation of distribution of attenuation in object's interior.

and to measure the reduction in beam intensity along each of those paths. In one commonly used configuration (Fig. 2), the object to be scanned is placed in a fan-beam of coplanar X-rays, whose attenuation upon passage through the object is measured by an arc of detectors. Attenuation measurements are made as the specimen rotates, which provides views of the object from multiple angles; from these data, a 2D image can be reconstructed that maps the linear X-ray attenuation coefficients in the object's interior, in the plane of the X-ray beam (Video 1). This image is the "slice" that gives tomography its name (from the Greek *tomos*: slice, section); it corresponds to what would be seen if the object were sliced along the scan plane. Stacking contiguous slices produces a 3D image, best visualized by means of isosurfacing, volume rendering, or animation; examples appear below.

XCT scanners implement this general strategy in a variety of different ways, reflecting the need to scan objects than span a range of sizes and densities. Higher-energy X-ray sources are needed to penetrate larger,

denser objects, and the achievable spatial resolution depends strongly on the scale of the object, due to restrictions on detector size and reconstruction methods. Conventional medical scanners use low-energy X-rays (≤ 125 keV), and are designed for low-dosage imaging of relatively low-density meter-scale objects at millimeter-scale resolution; they lack both the penetrating power and the spatial resolution required by many applications in the earth and planetary sciences. High-resolution and ultra-high-resolution industrial scanners use specialized X-ray tube sources with maximum energies roughly in the ranges of 300–450 keV and 150–250 keV respectively; they image decimeter- to centimeter-scale objects at spatial resolutions on the order of 100s to 10s of micrometers. Synchrotron X-ray sources provide highly collimated, intense beams that yield spatial resolution approaching $1 \mu\text{m}$ on specimens from centimeter- to millimeter-scale, using X-rays with relatively low energies, up to perhaps 50–90 keV. Because of the extraordinary brightness and brilliance of synchrotron-generated X-ray beams, diffractive



Video 1. [Online animation at doi:10.1016/j.epsl.2006.06.020]. Illustration of acquisition of single slice of XCT imagery and reconstruction of the 2D image by filtered backprojection. For more details of reconstruction process, consult [2,5]. *Top left panel* shows object to be scanned (fossil skull, externally prepared but filled with matrix), in the path of planar X-ray fan beam. *Top right panel* shows section through skull intersected by fan beam during object rotation. *Lower left panel* shows buildup of the "sinogram," an accumulation of the attenuation measurements of the fan beam over time (bright=high attenuation); during reconstruction, line marks the view currently being added to the backprojected image. *Lower right panel* shows progressive development of image as successive views are superposed during backprojection.

monochromators can be used to modify the X-ray beam so that it contains only photons of a single selected energy. This makes possible element-specific imaging. If an object is imaged twice, with monochromatic X-ray energies that lie above and below an absorption edge of a particular element of interest, subtraction of the two images will yield a map showing the distribution of only that element. X-ray fluorescence measurements can also be combined with positional data to create element-specific tomographic images.

Several factors may complicate the collection and interpretation of XCT imagery. X-ray attenuation at these energies arises from two processes. *Photoelectric absorption*, which is a very strong function of mean atomic number, dominates at energies up to about 50–100 keV; at higher energies, the predominant effect is *Compton scattering*, which is less strongly dependent on mean atomic number. As a result, compositional differences have a greater impact on XCT contrast at lower energies, whereas contrast at higher energies depends largely on differences in mass density. To image materials that differ in composition but not mass density, low-energy X-rays must be used, and these may be unable to penetrate thick specimens.

Several scanning artifacts may also affect XCT imagery, though in many cases their deleterious effects can be minimized or eliminated with proper scanning protocols. Principal among these artifacts is *beam-hardening*, an increase in the mean energy of a polychromatic X-ray beam that results from the greater attenuation of lower energy X-rays during passage through the object. Beam-hardening appears in XCT imagery as an artificial reduction of attenuation near the centers of long X-ray paths. Ring artifacts are circular variations in image brightness centered on the rotation axis; they typically arise from detector drift that degrades the ability of calibration measures to compensate for variations in the sensitivity of each individual detector. Both artifacts can greatly complicate quantitative analysis of images, because they cause the same material to be assigned different grayscale values depending on its position in the image. These artifacts can be minimized with proper beam-filtering or special scanning protocols (a “wedge” calibration; cf. [2, p. 388]); ring artifacts are often amenable to software correction prior to image reconstruction.

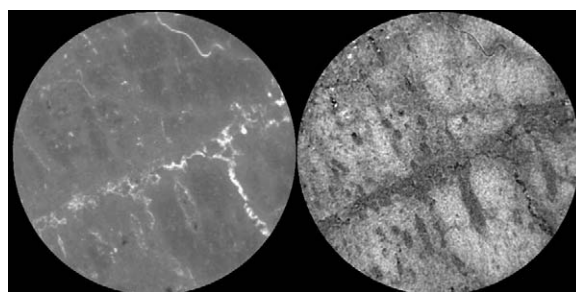
3.2. Applications in the earth and planetary sciences

The number and variety of research efforts in the earth and planetary sciences that use XCT have burgeoned rapidly in the last three years. A compre-

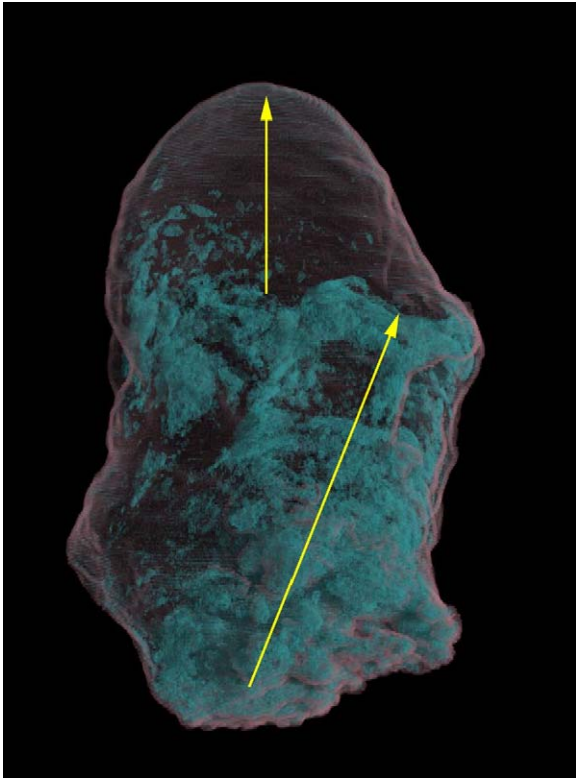
hensive review will not be attempted here; instead, a suite of examples is presented, with the intention of sampling the diverse range of recent applications. Brief descriptions of projects demonstrating the utility of XCT have been compiled in several reviews [2,6–8], and more thorough accounts have been collected in a recent symposium volume [9].

3.2.1. Hydrology, soil science, and environmental geology

XCT contributes to studies of fluid flow in porous media by virtue of its ability to discriminate between the mineral matrix and either the open porosity, fluid-filled pores and fractures (for which contrast may be enhanced by addition of a dopant with high attenuation), or mineral-filled altered/sheared zones of high permeability. Because flow depends on features that range in scale from macroscopic to microscopic, the full range of XCT instrumentation has been employed to image porous geological media [3], and investigations of pore structure, connectivity, and flow properties are numerous. Synchrotron-based microtomography reveals pore-scale features in exceptional detail, allowing quantitative characterization of pore geometries [10–12]. High-resolution CT studies can directly image the presence and connectivity of large-void and fracture porosity [13], and microfocal systems can measure variations in partial porosities across a range of microscopic and macroscopic scales, when images of a specimen in dry and saturated states are subtracted (Video 2) [14]. Images produced with conventional CT can map flow



Video 2. [Online animation at doi:10.1016/j.epsl.2006.06.020]. *Left panel* shows single slice from stack of contiguous high-resolution XCT images of altered volcanic rock from deep-sea hydrothermal field; slice is 57.8 μm thick, and diameter of field of view is 24 mm. Voids are dark, sulfide veins are bright. *Right panel* shows corresponding porosity map: bright regions have high porosity, dark regions have low porosity. This image resulted from subtraction of optimally registered images of dry and water-saturated core. Quantitative analyses can be performed on these maps, such as determining the frequency distribution of partial porosity and directional analysis to infer flow anisotropy [14].



Video 3. [Online animation at [doi:10.1016/j.epsl.2006.06.020](https://doi.org/10.1016/j.epsl.2006.06.020)]. Stalagmite with two growth axes; volume rendering from high-resolution XCT data. Maximum dimension=22 cm; for details, consult [25]. Solid material is rendered transparent to reveal inclusions, shown in blue. Inclusions mark two growth axes, shown by arrows, neither apparent from external visual examination. In paleoclimatic studies, samples for chemical and isotopic analysis must be taken from a growth axis to avoid unpredictable non-equilibrium fractionation effects; XCT can also reveal the internal location of large fluid inclusions for isotopic analysis.

characteristics averaged over macroscopic volumes [15–18].

The ability of XCT to image concentration differences for tracers of high atomic number has been exploited to measure the diffusivities of heavy ions in an artificial barrier material for nuclear-waste disposal [19], and the absorptive properties of aggregate soil samples for heavy-ion contaminants have been studied at grain scale with microtomography [20]. XCT has proven useful for determination of soil structure [21], tillage effects in soils [22], and experimental determination of void-ratio redistribution in soils during undrained compression [23]. The adsorption kinetics of CO₂ on coal, a factor in potential carbon-dioxide sequestration efforts, has been quantified by XCT imagery of controlled sorption experiments on consolidated specimens [24]. Knowledge from XCT of the 3D internal structure of speleothems (Video 3) ensures that isotopic and chemical analyses, which provide proxies for past climate change, are performed on pristine samples, those taken along the growth axis [25].

3.2.2. Paleontology

In the broad field of paleontology, XCT has had a transformative impact on morphological research in general and vertebrate studies in particular. The natural connection to medical CT made the scanning of vertebrate fossils one of the earliest applications of CT in the earth sciences. The advent of high-resolution scanners expanded those applications to an extraordinarily wide range of taxa, and an immense quantity of data on both fossil and modern organisms is now available in the literature and online: see, for example, <http://www.digimorph.org/>. Recent XCT studies in paleontology



Video 4. [Online animation at [doi:10.1016/j.epsl.2006.06.020](https://doi.org/10.1016/j.epsl.2006.06.020)]. Skull of *Tyrannosaurus rex*, isosurface image from XCT data. Maximum dimension=1.44 m; for details, consult [26].

range in scale from the skull of *Tyrannosaurus rex* (Video 4) [26] to the microarchitecture of echinoids [27], and include some of the world's most famous fossils (e.g., *Archaeopteryx* [28]) and some of its most infamous (e.g., *Archaeoraptor* [29]). As a non-destructive technique, XCT allows 3D examination of fossils too rare to be examined by serial sectioning, and those that for a variety of reasons cannot be prepared (extracted from their surroundings) by traditional means [30–34]. The 3D digital character of XCT data has led to novel discoveries by enabling representation of internal morphological features that are otherwise impractical or impossible to obtain (e.g., cranial endocasts) [35], and it facilitates digital construction of physical replicas of specimens that would otherwise remain inaccessible [36].

3.2.3. Petroleum geology and sedimentology

XCT has become a widely employed tool in the oil and gas industry for characterization of the petrophysical features of hydrocarbon reservoir rocks [37–39], not only in the context of fluid flow [6] but also as means of evaluating reservoir quality [40–42]. Characterization of sedimentary structures in 3D requires features that display distinct density contrast with their surroundings (e.g., sand dikes, dropstones and plant remains in lake sediments [43]).

3.2.4. Petrology

Many petrologic studies derive information from rocks' textures and fabrics, and traditional approaches based on examination of sawn surfaces, thin sections, or other 2D techniques are now being supplemented or

supplemented by 3D data derived from XCT. An early application of high-resolution XCT was quantitative analysis of metamorphic textures to identify crystallization mechanisms and quantify reaction kinetics (Video 5) [44], and improvements in CT technology (and in analytical methods) have refined and expanded this line of research [45–47]. Visualization and quantification of the spatial configuration of crystals and melt have led to new understanding of permeability and melt flow in basaltic magmas [48] and in migmatites [49]. Specialized scanning protocols that yield high contrast for diamond in eclogites have revealed that diamond is invariably associated with secondary metasomatic phases; it thus postdates formation of the eclogitic assemblage and records an important part of a complex history of mantle metasomatism [50,51]. Many geochemical and geochronological analyses benefit from the use of XCT to locate phases in a 3D context, maximizing the information that can be derived when they are later extracted or precisely sectioned; for example, garnet porphyroblasts can be cut and polished through their morphological centers and exactly perpendicular to rotation axes for chemical and structural analysis [52]. The development of apparatus for synchrotron microtomography at pressures up to 8 GPa opens up striking possibilities for *in-situ* experimental investigations of microstructures at high pressure and during deformation [53].

3.2.5. Geodynamics and structural geology

Diverse applications in geodynamics and structural geology reflect the versatility of XCT. Precise data in 3D on the difference in modal vesicle sizes between the



Video 5. [Online animation at [doi:10.1016/j.epsl.2006.06.020](https://doi.org/10.1016/j.epsl.2006.06.020)]. Porphyroblastic garnet–kyanite schist; volume renderings from high-resolution CT scans. Maximum dimension = 12 cm. *Left panel* shows pseudocolored 3D reconstruction in which all phases are opaque: garnets are pink, kyanite laths are blue, biotite-kyanite-rich regions are dark gray to black, and quartz-rich regions are light gray. *Right panel* shows pseudocolored 3D reconstruction with a transparent matrix, leaving only the garnet porphyroblasts visible. Object-mensuration software allows statistical analysis of porphyroblast sizes and locations in 3D, which identify reaction mechanisms and quantify reaction kinetics [45].

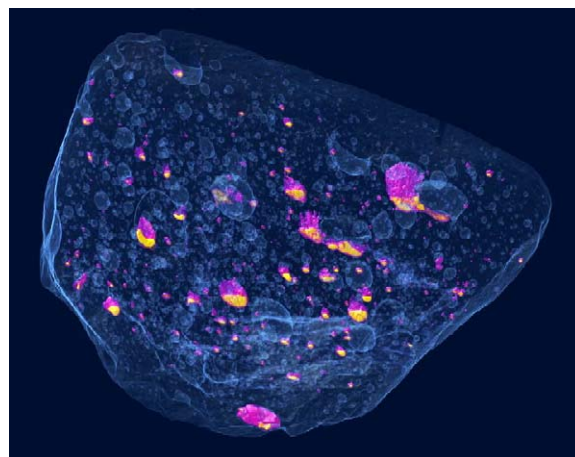
tops and bottoms of basalt flows allow estimation of paleoelevations at the time of emplacement; in combination with radiometric ages of the flows, these data yield quantitative rates of regional uplift [54,55]. Analog models of natural structures can be imaged rapidly enough in modern CT instruments to permit 4D analysis (time sequences of 3D images) of deformation patterns and processes [56]. At the scale of individual porphyroblasts, the 3D shapes of inclusion trails can be visualized to test theories of grain-scale deformation and its relation to local and regional stress fields [57].

3.2.6. Engineering geology and economic geology

A comparable range of utility for XCT exists in engineering and economic geology. Controls on the post-compaction settlement behavior of materials used for backfilling of excavations were elucidated by scanning of mudrock subjected to experimental compaction [58]. The discovery by XCT of contrasting drying behaviors for sandstones, depending on whether they are fully saturated or merely wetted by capillary absorption, has implications for curators and restorers of building stones [59]; patterns of water penetration into building stone can also be assessed by XCT [60]. Images of fracture surfaces in 3D have been used to verify numerical models that predict the fracture response of rock masses to planned excavation shapes in deep mines [61]. Mechanisms that result in high-grade veins in ore districts were revealed by high-resolution XCT images of individual gold-bearing grains; measurements of their dimensional anisotropy and orientations related their origin to regional stress fields [62].

3.2.7. Meteoritics and planetary science

Non-destructive methods hold obvious advantages for rare meteorites and other planetary materials, so XCT can play a vital role in their curation and study. When present, metal phases and vesicles offer marked contrast to silicate hosts, a fact that has been widely exploited by 3D imaging and quantification. For instance, in an unusual lodranite, high-resolution XCT imaging linked metal segregations containing graphite rosettes to a suite of metal veins amidst a variably metal-depleted matrix, revealing details of likely processes of melt generation and migration during core formation; the imagery also guided stable isotopic investigations that uncovered extraordinary heterogeneity [63]. Visualization in 3D of the internal structures of a metal-bearing meteorite breccia provided evidence of impact-induced melting and metamorphism in an ordinary chondrite [64]. High-resolution XCT of rare vesicular basaltic meteorites (Video 6) quantified bubble sizes and distributions,



Video 6. [Online animation at doi:10.1016/j.epsl.2006.06.020]. Spatial relationship between vesicles and metal/sulfide particles in rare vesicular meteorite (impact melt of ordinary chondrite); volume rendering from high-resolution XCT data. Maximum dimension=15 cm; for details, consult [68]. Components of the meteorite other than vesicles and metal/sulfide particles have been rendered transparent; the outer surface and vesicle walls are blue, metal is violet, sulfide is orange. The association of vesicles with the particles, and the fact that all metal-sulfide contacts have the same 3D orientation, support the hypothesis that the vesicles once held SO₂ formed by vaporization of FeS during impact melting of Fe,Ni metal and sulfide.

leading to detailed inferences regarding the types and concentrations of the volatile gases that formed the vesicles, the depths at which melts formed, moved, and solidified, and the role of bubble coalescence, all of which differ among vesicular eucrites [65], angerites [66], and impact melts of ordinary chondrites [67].

High-resolution XCT examination of an impact breccia determined the 3D distribution of four distinct populations of clasts and quantified their abundances [68]. Images of individual chondrules in CR2 chondrites demonstrated that 3D data are vital to determine accurately the abundance and distribution of metal within them, and their degrees of sphericity, for characterization of their extents of melting and chemical maturation [69]. Microtomography of several hundred lunar glass spherules located and identified a contained olivine phenocryst, several inclusions of metal grains, and voids [70], and calcium–aluminum-rich inclusions (CAIs) in CV3 chondrites were similarly identified and located to permit exposure for chemical analysis by sectioning [71].

4. Neutron tomography

NCT is similar in many ways to XCT; it measures the attenuation of an incident neutron beam along a

variety of intersecting paths through the specimen and uses those measurements to reconstruct the internal distribution of materials with contrasting neutron attenuation coefficients. Because hydrogen is among the most effective attenuators of neutrons, but produces almost negligible X-ray attenuation, the information available from NCT is often complementary to that of XCT in this regard (Fig. 3) [72].

4.1. Technical principles

Most neutron tomography is performed using collimated polychromatic “thermal” (mean energy ~ 25 meV) or “cold” (~ 0.5 – 2 meV) neutron beams; these are generated by either nuclear research reactors or spallation sources, which are accelerator-driven. An intriguing aspect of NCT is that because some metals (notably Al, but not Fe) have very low cross-sections for neutron scattering, and thus are nearly transparent to neutron irradiation, it is possible to conduct *in-situ* tomographic studies of specimens housed in various types of experimental apparatus. Such housings often impair or prevent XCT imaging because of their high X-ray attenuation.

One obstacle to widespread application of NCT has been its limited spatial resolution; in most implementations, the best resolution that can be achieved is no better than ~ 100 μm . The resolution depends primarily upon the divergence of the beam from its nominally parallel geometry, which varies with neutron energy, and upon the characteristics of the detector system (typically a scintillator screen) that converts beam intensity into an electromagnetic signal. The neutron beams used for tomography are commonly polychromatic (that is, they

contain neutrons with a spread of energies), which leads to artifacts in the imagery analogous to beam-hardening artifacts in XCT. Because nearly all neutron attenuation by hydrogen is due to scattering, significant noise arises in NCT images in hydrogen-rich specimens.

4.2. Applications in the earth and planetary sciences

Beamlines suitable for neutron tomography began to appear at research facilities only in the late 1990s, so optimal imaging protocols are still under development, and applications in the earth sciences, beyond small feasibility studies, are few. NCT has been used to generate 3D images of muscovite in pegmatite, zeolite-lined cavities in basanite, and garnet crystals (neutron-transparent) in a fine-grained micaceous matrix (neutron-absorbent) [73]. A similar proof-of-principle study allowed 3D visualization of water infusion in building stone, differentiating between rapid exterior uptake and more sluggish interior uptake [74]. Relationships between pore geometry and degree of water saturation were determined in a quartz arenite [75], and NCT was used to visualize two-phase flow in a fault-gouge-filled fracture in granodiorite during capillary imbibition and subsequent drainage by air injection [76]. Differences in compaction, water content and water distribution in soils have been imaged and measured [77]. NCT has documented 3D interconnectivity of diagenetic calcite-filled veins in shale [78].

5. Magnetic resonance imaging

Like XCT, MRI originated as a medical diagnostic tool, becoming widely implemented in the 1980s. Near

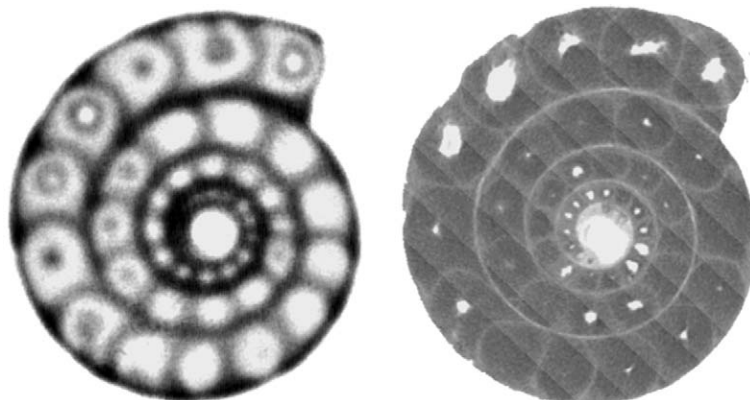


Fig. 3. Pyritized ammonite imaged by NCT (left) and by XCT (right); from [73]. Maximum dimension = 21 mm. Outer surface and thin septa between chambers are altered to iron hydroxides; neutron attenuation from these H-bearing phases produces the contrast in the NCT image. Small differences in mass density produce the weaker contrast in the XCT image. (Note that the polarity in this image is reversed from normal XCT convention; normally, more attenuating materials are brighter, but here the opposite is true.)

that decade's end, improvements in resolution marked the advent of magnetic resonance microscopy, and following increases in sensitivity in the 1990s, applications began to emerge in engineering and materials science, then eventually in the geosciences. A readable introduction to the technique can be found in Nestle et al. [79]; the classic text by Callaghan [80] contains full details.

5.1. Technical principles

The principle underlying MRI is that the position of a nucleus in a magnetic field gradient influences the character of its magnetic resonance (MR). Time-varying magnetic gradients in three orthogonal directions, coupled with radio-frequency (RF) pulses, are applied repetitively to the sample in a progression that encodes spatial information into the MR response, the output signal that results from the relaxation of the spin realignments induced by the imposed fields. Each point in the specimen contributes to the resonance signal a component with frequency and phase specific

to that point's location in the specimen, and an amplitude that contains information on the *nuclear spin density* there. But the amplitude also depends on the parameters used to define the progression of applied magnetic-field gradients and RF pulses (the *imaging sequence*) and the local MR relaxation times. Those relaxation times are sensitive functions of the physical environment of the nucleus (whether it makes up a free fluid, is adsorbed on a mineral surface, is present in larger or smaller pores, etc.) and its chemical environment (whether it is present in polar or nonpolar liquid, the concentration of any dissolved paramagnetic ions, etc.). These factors complicate the interpretation of MR imagery, but also present opportunities to use MRI to probe subtle physicochemical aspects of specimens. Because the MR response is also modulated by physical motion of the nucleus, specialized MRI methods are capable of directly imaging the flow and diffusion of fluids.

Resolution in MRI depends upon the strength of the applied gradients, the nuclear spin density, and the transverse relaxation rate, which characterizes the width of

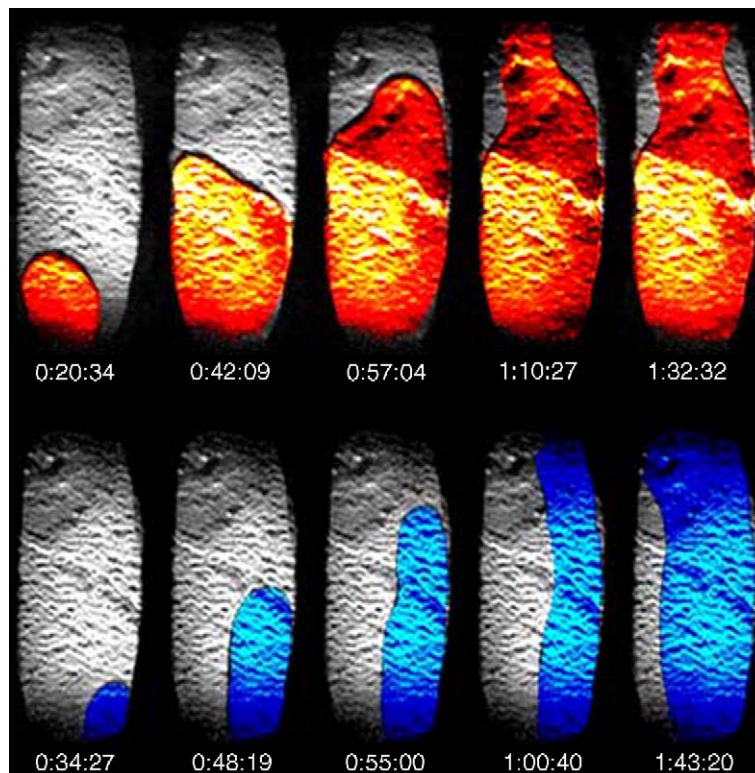


Fig. 4. Time series of MRI images comparing flow of light NAPL (dodecane, *top*, in orange) and dense NAPL ("Fluorinert" FC-75, *bottom*, in blue) through water-saturated fracture in dolomite core. Maximum dimension = 10 cm. The effects of buoyancy differences between the two contaminants (e.g., dense NAPL favoring the right side of the fracture, which is lower) and the aperture distribution (e.g., spreading of the light NAPL along diagonal fracture offset, followed by breakthrough) are evident. Original publication [89] includes animations.

the frequency signal; at present, millimeter-scale resolution is commonplace using conventional clinical instruments, and resolution approaching 10 μm has been demonstrated on a dedicated research instrument [81]. Magnetic impurities in the specimen, spatially varying concentrations of paramagnetic materials, and local variations in magnetic susceptibility (e.g., bubbles) introduce internal magnetic field gradients and heterogeneities that may produce serious distortion and signal attenuation, rendering some specimens unsuitable for MRI.

5.2. Applications in the earth and planetary sciences

Although other nuclei of high abundance with unpaired nuclear spins (e.g., ^{19}F , ^{23}Na , ^{31}P , ^{39}K) may be of interest in some studies, the great bulk of MRI in the earth and planetary sciences uses ^1H , which has the highest magnetic moment of all stable nuclei. However, hydrogen in rigid solid phases does not yield a detectable signal in standard MRI, so the technique is strongly focused on fluids. Reports in the recent literature have begun to move beyond feasibility studies to applications, principally concerning subsurface residence and transport of water, dissolved substances, and contaminants (including NAPLs) in soils, sediments, and fractured rock.

The 3D geometry of sedimentary structures and trace fossils that influence dolomitization and porosity development in carbonate hydrocarbon reservoirs have been imaged by MRI [82], and porosity distribution in worm-burrowed sandstones has likewise been studied [83]. An example in the environmental sciences is an MRI study of soil-wetting processes affecting the uptake of pesticides [84]. Direct observation by MRI of the flow and diffusion of pore water in synthetic porous media [85] complements studies that use paramagnetic tracers to study transport in such systems [86]. MRI has allowed visualization of the imbibition of water into fractured porous sandstone and measurement of local water saturation values within it [87], as well as observation of the flow of dense and light NAPLs through a water-saturated fracture in dolomite (Fig. 4) [88]. A unique twist on the technique is work that used MRI to image changes in granular microstructure in dense shear flows by using oil-rich seeds as analogs to geoparticles; the oils in the seeds supply the free protons needed for MRI imaging [89]. The potential for very high-resolution work using specially designed research instruments is demonstrated by a micropaleontological feasibility study imaging the 3D morphology of radiolaria [81]. Novel MRI studies of the thermal

evolution of pore microstructures in sea-ice have also begun to appear [90,91].

6. Future directions

Three-dimensional imaging originated from breakthroughs in technology, so it is reasonable to expect that future directions will be determined by further technological innovations.

In terms of XCT, further development of “desktop” microfocal systems for centimeter-scale samples could soon lead to such systems becoming as common in research institutions as SEMs or X-ray powder diffractometers, and their use could become a routine aspect of many studies. Higher-energy microfocal systems should evolve toward still higher spatial resolution and faster scan times, as source and detector technology improves; increases in the energy of synchrotron sources at microtomography beamlines should enable analysis of larger, denser specimens at micron-scale resolution. Both of these developments will result in massive data volumes for 3D imagery, requiring commensurate increases in computational power for data analysis. Already it appears that XCT has matured to the point where tomographic reconnaissance should be a routine part of the accession protocol for collections of rare materials such as fossils, meteorites, and the products of extraterrestrial sample-return missions.

NCT in the earth and planetary sciences appears poised to take major steps forward. Methods for reduction of scattering artifacts in NCT imagery are under development [92]. With the advent of techniques using a focusing neutron lens, neutron microtomography should soon become possible on small specimens [93]. Experiments with neutron-velocity selectors (to eliminate low-energy beam components with relative strong divergence) and thinner scintillators (to minimize the spread of light in the detector) portend improvements in spatial resolution for larger specimens [94]. Energy-selective imaging using monochromatized neutron beams should allow the probe used for NCT to be optimized for particular imaging tasks [95]. Substantial advances in detector technology may lead to significant improvements in spatial resolution [96].

Likely paths for future development of MRI in the geosciences are less clear. One evident need arises from the short relaxation times that prevent imaging of many features of geological interest. Although some specialized MRI techniques hold promise in this regard, overcoming this difficulty will likely require hardware

developments to allow more intense magnetic field gradients, stronger gradient pulses, and the ability to switch fields in shorter times [79].

In the past, the primary drivers for innovation in 3D imaging have come from medical or engineering applications. Although that will no doubt continue, demand based on geoscience applications of these techniques has now led to the development of specially optimized instruments, and the establishment of dedicated facilities. That specialization will continue to accelerate the expansion in the depth and breadth of results from 3D imaging in the earth and planetary sciences.

Acknowledgements

Figures in the section on XCT were prepared by Rich Ketcham and the staff of the University of Texas High-Resolution X-ray Computed Tomography Facility, which is supported by U.S. National Science Foundation Grant EAR-0345710. Dawn Sumner graciously provided numerous valuable clarifications, and Alex Halliday is thanked for his most helpful and patient editorial role.

References

- [1] R.A. Ketcham, Computational methods for quantitative analysis of three-dimensional features in geological specimens, *Geosphere* 1 (2005) 32–41.
- [2] R.A. Ketcham, W.D. Carlson, Acquisition, optimization and interpretation of X-ray computed tomographic imagery: applications to the geosciences, *Comput. Geosci.* 27 (2001) 381–400.
- [3] D. Wildenschild, J.W. Hopmans, C.M.P. Vaz, M.L. Rivers, D. Rickard, B.S.B. Christensen, Using X-ray computed tomography in hydrology: systems, resolutions, and limitations, *J. Hydrol.* 267 (2002) 285–297.
- [4] ASTM, Standard Guide for Computed Tomographic (CT) Imaging, ASTM Designation E1441-92a, 1992 Annual Book of ASTM Standards, Section 3, Metals Test Methods and Analytical Procedures, ASTM, Philadelphia, 1992, pp. 690–713.
- [5] A.C. Kak, M. Slaney, Principles of Computerized Tomographic Imaging, Society for Industrial and Applied Mathematics, Philadelphia, 2001, 327 pp.
- [6] S. Akin, A.R. Kovscek, Computed tomography in petroleum engineering research, in: F. Mees, R. Swennen, M. Van Geet, P. Jacobs (Eds.), Applications of X-ray Computed Tomography in the Geosciences, Special Publication, vol. 215, Geological Society, London, 2003, pp. 23–38.
- [7] W.D. Carlson, T. Rowe, R.A. Ketcham, M.W. Colbert, Applications of high-resolution X-ray computed tomography in petrology, meteoritics and palaeontology, in: F. Mees, R. Swennen, M. Van Geet, P. Jacobs (Eds.), Applications of X-ray Computed Tomography in the Geosciences, Special Publication, vol. 215, Geological Society, London, 2003, pp. 7–22.
- [8] S.R. Sutton, P.M. Bertsch, M. Newville, M. Rivers, A. Lanzirotti, P. Eng, Microfluorescence and microtomography analyses of heterogeneous earth and environmental materials, *Rev. Mineral. Geochem.* 49 (2002) 429–483.
- [9] F. Mees, R. Swennen, M. Van Geet, P. Jacobs (Eds.), Applications of X-ray Computed Tomography in the Geosciences, Special Publication, vol. 215, Geological Society, London, 2003, 243 pp.
- [10] R.I. Al-Raoush, C.S. Willson, Extraction of physically realistic pore network properties from three-dimensional synchrotron X-ray microtomography images of unconsolidated porous media systems, *J. Hydrol.* 300 (2005) 44–64.
- [11] K.W. Jones, H. Feng, W.B. Lindquist, P.M. Adler, J.F. Thovert, B. Vekemans, L. Vincze, I. Szaloki, R. Van Grieken, F. Adams, C. Riekel, Study of the microgeometry of porous materials using synchrotron computed microtomography, in: F. Mees, R. Swennen, M. Van Geet, P. Jacobs (Eds.), Applications of X-ray Computed Tomography in the Geosciences, Special Publication, vol. 215, Geological Society, London, 2003, pp. 39–49.
- [12] D. Wildenschild, J.W. Hopmans, M.L. Rivers, A.J.R. Kent, Quantitative analysis of flow processes in a sand using synchrotron-based X-ray microtomography, *Vadose Zone Journal* 4 (2005) 112–126.
- [13] K. Vandersteen, B. Busselen, K. Van Den Abeele, J. Carmeliet, Quantitative characterizations of fracture apertures using micro-focus computed tomography, in: F. Mees, R. Swennen, M. Van Geet, P. Jacobs (Eds.), Applications of X-ray Computed Tomography in the Geosciences, Special Publication, vol. 215, Geological Society, London, 2003, pp. 61–68.
- [14] R.A. Ketcham, G.J. Iturrino, Nondestructive high-resolution visualization and measurement of anisotropic effective porosity in complex lithologies using high-resolution X-ray computed tomography, *J. Hydrol.* 302 (2005) 92–106.
- [15] S.H. Anderson, H.F. Wang, R.L. Peyton, C.J. Gantzer, Estimation of porosity and hydraulic conductivity from X-ray CT-measured solute breakthrough, in: F. Mees, R. Swennen, M. Van Geet, P. Jacobs (Eds.), Applications of X-ray Computed Tomography in the Geosciences, Special Publication, vol. 215, Geological Society, London, 2003, pp. 135–149.
- [16] M. Cislérova, J. Votrubová, CT derived porosity distribution and flow domains, *J. Hydrol.* 267 (2002) 186–200.
- [17] Y. Géraud, F. Surma, F. Mazerolle, Porosity and fluid flow characterization of granite by capillary wetting using X-ray computed tomography, in: F. Mees, R. Swennen, M. Van Geet, P. Jacobs (Eds.), Applications of X-ray Computed Tomography in the Geosciences, Special Publication, vol. 215, Geological Society, London, 2003, pp. 95–105.
- [18] T. Hirono, M. Takahashi, S. Nakashima, Direct imaging of fluid flow in fault-related rocks by X-ray CT, in: F. Mees, R. Swennen, M. Van Geet, P. Jacobs (Eds.), Applications of X-ray Computed Tomography in the Geosciences, Special Publication, vol. 215, Geological Society, London, 2003, pp. 107–115.
- [19] Y. Nakashima, Diffusivity measurement of heavy ions in Wyoming montmorillonite gels by X-ray computed tomography, *J. Contam. Hydrol.* 61 (2003) 147–156.
- [20] S.J. Altman, M.L. Rivers, M.D. Reno, R.T. Cygan, A.A. McLain, Characterization of adsorption sites on aggregate soil samples using synchrotron X-ray computerized microtomography, *Environ. Sci. Technol.* 39 (2005) 2679–2685.
- [21] H. Rogasik, I. Onaschi, J. Brunotte, D. Jegou, O. Wendroth, Assessment of soil structure using X-ray computed tomography, in: F. Mees, R. Swennen, M. Van Geet, P. Jacobs (Eds.), Applications of X-ray Computed Tomography in the

- Geosciences, Special Publication, vol. 215, Geological Society, London, 2003, pp. 151–165.
- [22] C.J. Gantzer, S.H. Anderson, Computed tomographic measurement of macroporosity in chisel-disk and no-tillage seedbeds, *Soil Tillage Res.* 64 (2002) 101–111.
- [23] P.R. Thomson, R.C.K. Wong, Monitoring void ratio redistribution during continuous undrained triaxial compression by X-ray computed tomography, in: F. Mees, R. Swennen, M. Van Geet, P. Jacobs (Eds.), Applications of X-ray Computed Tomography in the Geosciences, Special Publication, vol. 215, Geological Society, London, 2003, pp. 191–198.
- [24] C.Ö. Karacan, An effective method for resolving spatial distribution of adsorption kinetics in heterogeneous porous media: application for carbon dioxide sequestration in coal, *Chem. Eng. Sci.* 58 (2003) 4681–4693.
- [25] P.J. Mickler, R.K. Ketcham, M.W. Colbert, J.L. Banner, Application of high-resolution X-ray computed tomography in determining the suitability of speleothems for use in paleoclimatic, paleohydrologic reconstructions, *J. Caves Karst Stud.* 66 (2004) 4–8.
- [26] C.A. Brochu, Osteology of *Tyrannosaurus rex*: insights from a nearly complete skeleton and high-resolution computed tomographic analysis of the skull, *J. Vertebr. Paleontol.* 22 (Supplement 4) (2003) 138 pp.
- [27] S.R. Stock, A. Veiss, Preliminary microfocus X-ray computed tomography survey of echinoid fossil microstructure, in: F. Mees, R. Swennen, M. Van Geet, P. Jacobs (Eds.), Applications of X-ray Computed Tomography in the Geosciences, Special Publication, vol. 215, Geological Society, London, 2003, pp. 225–235.
- [28] P. Dominguez Alonso, A.C. Milner, R.A. Ketcham, M.J. Cookson, T.B. Rowe, The avian nature of the brain and inner ear of *Archaeopteryx*, *Nature* 430 (2004) 666–669.
- [29] T. Rowe, R.A. Ketcham, C. Denison, M. Colbert, X. Xu, P.J. Currie, The Archaeopteryx forgery, *Nature* 410 (2001) 539–540.
- [30] J.E. Clack, P.E. Ahlberg, S.M. Finney, P. Dominguez Alonso, J. Robinson, R.A. Ketcham, A uniquely specialized ear in a very early tetrapod, *Nature* 425 (2003).
- [31] M. Kearney, J.A. Maisano, T. Rowe, Cranial anatomy of the extinct amphisbaenian *Rhineura hatcherii* (Squamata, Amphisbaenia) based on high-resolution X-ray computed tomography, *J. Morphol.* 264 (2005).
- [32] M.J. Polcyn, L.L. Jacobs, A. Haber, A morphological model and CT assessment of the skull of *Pachyrhachis problematicus* (Squamata, Serpentes), a 98 million year old snake with legs from the Middle East, *Palaeontol. Electronica* 8 (2005) 26.
- [33] M.J. Polcyn, J.V.J. Rogers, Y. Kobayashi, L.L. Jacobs, Computed tomography of an Anolis lizard in Dominican amber: systematic, taphonomic, biogeographic, and evolutionary implications, *Palaeontol. Electronica* 5 (2002) 13.
- [34] M.J. Vendrasco, T.E. Wood, B.N. Runnegar, Articulated Paleozoic fossil with 17 plates greatly expands disparity of early chitons, *Nature* 429 (2004) 288–291.
- [35] L.M. Witmer, S. Chatterjee, J.W. Franzosa, T. Rowe, Neuroanatomy of flying reptiles, and implications for flight, posture, and behavior, *Nature* 425 (2003) 950–953.
- [36] A.M. Torres, A.M. Christensen, T.E. Masters, R.A. Ketcham, A uniquely specialized ear in a very early tetrapod, *Nature* 425 (2003) 65–69.
- [37] C.H. Arns, A. Sakellariou, T.J. Senden, A.P. Sheppard, R.M. Sok, W.V. Pinczewski, M.A. Knackstedt, Petrophysical properties derived from X-ray CT images, *APPEA J.* 43 (2003) 577–585.
- [38] A.S. Grader, M. Balzarini, F. Radaelli, G. Capasso, A. Pellegrino, Fracture-matrix flow: quantification and visualization using X-ray computerized tomography, dynamics of fluids in fractured rock, *AGU Geophys. Monogr.* 122 (2000) 157–168.
- [39] M.A. Knackstedt, C.H. Arns, A. Limaye, A. Sakellariou, T.J. Senden, A.P. Sheppard, R.M. Sok, W.V. Pinczewski, G.F. Bunn, Digital core laboratory; reservoir-core properties derived from 3D images, *J. Pet. Technol.* 56 (2004) 66–68.
- [40] C.Ö. Karacan, A.S. Grader, P.M. Halleck, Evaluation of local porosity changes in limestone samples under triaxial stress field by using X-ray computed tomography, in: F. Mees, R. Swennen, M. Van Geet, P. Jacobs (Eds.), Applications of X-ray Computed Tomography in the Geosciences, Special Publication, vol. 215, Geological Society, London, 2003.
- [41] M. Van Geet, D. Lagrou, R. Swennen, Porosity measurements of sedimentary rocks by means of microfocus X-ray computed tomography (μ CT), in: F. Mees, R. Swennen, M. Van Geet, P. Jacobs (Eds.), Applications of X-ray Computed Tomography in the Geosciences, Special Publication, vol. 215, Geological Society, London, 2003, pp. 51–60.
- [42] M. Van Geet, R. Swennen, M. Wevers, Quantitative analysis of reservoir rocks by microfocus X-ray computerised tomography, *Sediment. Geol.* 132 (2000) 25–36.
- [43] A. Flisch, A. Becker, Industrial X-ray computed tomography studies of lake sediment drill cores, in: F. Mees, R. Swennen, M. Van Geet, P. Jacobs (Eds.), Applications of X-ray Computed Tomography in the Geosciences, Special Publication, vol. 215, Geological Society, London, 2003, pp. 205–212.
- [44] W.D. Carlson, C. Denison, Mechanisms of porphyroblast crystallization: results from high-resolution computed X-ray tomography, *Science* 257 (1992) 1236–1239.
- [45] L.P. Baumgartner, C.T. Foster, T. Mueller, T. Vennemann, Reaction mechanism in siliceous dolomite contact aureoles; tabular olivine growth, *Geol. Soc. Am. Abstr. Prog.* 35 (2003) 226.
- [46] R.J. Clark, C.T. Foster Jr., B.L. Dutrow, Garnet crystal size and spatial distributions in a staurolite schist, *Geol. Soc. Am. Abstr. Prog.* 36 (2004) 42.
- [47] R.A. Ketcham, C.E. Meth, D. Hirsch, W.D. Carlson, Improved methods for quantitative analysis of three-dimensional porphyroblastic textures, *Geosphere* 1 (2005) 42–59.
- [48] T. Hersum, M. Hilpert, M. Marsh, Permeability and melt flow in simulated and natural partially molten basaltic magmas, *Earth Planet. Sci. Lett.* 237 (2005) 798–814.
- [49] M.A. Brown, M. Brown, W.D. Carlson, C. Denison, Topology of syntectonic melt flow networks in the deep crust: inferences from three-dimensional images of leucosome geometry in migmatites, *Am. Mineral.* 84 (1999) 1793–1818.
- [50] M. Anand, L.A. Taylor, K.C. Misra, W.D. Carlson, N.V. Sobolev, Nature of diamonds in Yakutian eclogites: views from eclogite tomography and mineral inclusions in diamond, *Lithos* 77 (2004) 333–348.
- [51] K.C. Misra, M. Anand, L.A. Taylor, N. Sobolev, Multi-stage metasomatism of diamondiferous eclogite xenoliths from the Udachnaya kimberlite pipe, Yakutia, Siberia, *Contrib. Mineral. Petrol.* 146 (2004) 696–714.
- [52] C.E. Meth, W.D. Carlson, Diffusion-controlled synkinematic growth of garnet from a heterogeneous precursor at Passo del Sole, Switzerland, *Can. Mineral.* 43 (2005) 157–182.
- [53] Y. Wang, T. Uchida, F. Westferro, M. Rivers, N. Nishiyama, J. Gebhardt, C.E. Lesher, S.R. Sutton, High-pressure X-ray

- tomography microscope: synchrotron computed microtomography at high pressure and temperature, *Rev. Sci. Instrum.* 76 (2005) 073709.
- [54] D. Sahagian, A. Proussevitch, W. Carlson, Timing of Colorado Plateau uplift: initial constraints from vesicular basalt-derived paleoelevations, *Geology* 30 (2002) 807–810.
- [55] D.L. Sahagian, A.A. Proussevitch, W.D. Carlson, Analysis of vesicular basalts and lava emplacement processes for application as a paleobarometer/paleoaltimeter, *J. Geol.* 110 (2002) 671–685.
- [56] G. Schreurs, R. Hänni, M. Panien, P. Vock, Analysis of analogue models by helical X-ray computed tomography, in: F. Mees, R. Swennen, M. Van Geet, P. Jacobs (Eds.), *Applications of X-ray Computed Tomography in the Geosciences*, Special Publication, vol. 215, Geological Society, London, 2003, pp. 213–223.
- [57] C.R. Huddleston-Holmes, R.A. Ketcham, Getting the inside story: using computed X-ray tomography to study inclusion trails in garnet porphyroblasts, *Am. Mineral.* 90 (2005) ea1–ea17.
- [58] M.A. O'Neill, A.K. Goodwin, W.F. Anderson, The use of X-ray computed tomography in the investigation of the settlement behaviour of compacted mudrock, in: F. Mees, R. Swennen, M. Van Geet, P. Jacobs (Eds.), *Applications of X-ray Computed Tomography in the Geosciences*, Special Publication, vol. 215, Geological Society, London, 2003, pp. 199–204.
- [59] B. Rousset-Tournier, F. Mazerolle, Y. Géraud, D. Jeannette, Rock drying tests monitored by X-ray computed tomography — the effect of saturation methods on drying behaviour, in: F. Mees, R. Swennen, M. Van Geet, P. Jacobs (Eds.), *Applications of X-ray Computed Tomography in the Geosciences*, Special Publication, vol. 215, Geological Society, London, 2003, pp. 117–125.
- [60] V.G. Ruiz de Argandoña, A. Rodríguez-Rey, C. Celorio, L. Calleja, L.M. Suárez del Río, Characterization by X-ray computed tomography of water absorption in a limestone used as a building stone in the Oviedo Cathedral (Spain), in: F. Mees, R. Swennen, M. Van Geet, P. Jacobs (Eds.), *Applications of X-ray Computed Tomography in the Geosciences*, Special Publication, vol. 215, Geological Society, London, 2003, pp. 127–134.
- [61] E. Sellers, A. Vervoort, J. Van Cleynebreugel, Three-dimensional visualization of fractures in rock test samples, simulating deep level mining excavation, using X-ray computed tomography, in: F. Mees, R. Swennen, M. Van Geet, P. Jacobs (Eds.), *Applications of X-ray Computed Tomography in the Geosciences*, Special Publication, vol. 215, Geological Society, London, 2003.
- [62] J.R. Kyle, R.A. Ketcham, In-situ distribution of gold ores using high-resolution X-ray computed tomography, *Econ. Geol.* 98 (2003) 1697–1701.
- [63] T.J. McCoy, W.D. Carlson, L.R. Nittler, R.M. Stroud, D.D. Bogard, D.H. Garrison, Graves Nunataks 95209: a snapshot of metal segregation and core formation, *Geochim. Cosmochim. Acta* 70 (2006) 516–531.
- [64] A.E. Rubin, F. Ulf-Møller, J.T. Wasson, W.D. Carlson, The Portales Valley meteorite breccia: evidence for impact-induced melting and metamorphism of an ordinary chondrite, *Geochim. Cosmochim. Acta* 65 (2001) 323–342.
- [65] T.J. McCoy, L. Wilson, G.K. Bendix, R.A. Ketcham, M. Wadhwa, A.M. Davis, Vesicular eucrites: where and how did they form and why are they so rare? Lunar and Planetary Science Conference, vol. 34, 2003, Abstr. No. 1187.
- [66] T.J. McCoy, L. Wilson, G.K. Bendix, R.A. Ketcham, Vesicles in meteorites: the angle on angrites, 66th Annual Meteoritical Society Meeting, Abstr. No. 5115, 2003.
- [67] G.K. Bendix, R.A. Ketcham, T.J. McCoy, L. Wilson, Vesiculation in ordinary chondrites due to impact melting: the “PAT” 91501 answers, Lunar and Planetary Science Conference, vol. 34, 2003, Abstr. No. 1947.
- [68] C. Koeberl, C. Denison, R.A. Ketcham, W.U. Reimold, High-resolution X-ray computed tomography of impactites, *J. Geophys. Res.* 107-E10 (2002) 5089.
- [69] J. Hertz, D.S. Ebel, M.K. Weisberg, Tomographic study of shapes and metal abundances of Renazzo chondrules, Lunar and Planetary Science Conference, vol. 34, 2003, Abstr. No. 1959.
- [70] D.S. Ebel, R.A. Fogel, M.L. Rivers, Tomographic location of potential melt-bearing phenocrysts in lunar glass spherules, . Lunar and Planetary Science Conference, vol. 36, 2005, Abstr. No. 1505.
- [71] J.M. Friedrich, K.P. Jochum, D.S. Ebel, First results of a physicochemical survey of CV3 calcium–aluminum-rich inclusions: the refractory trace elements Sr, Y, Zr, Nb, Ba, Hf, Ta, . Lunar and Planetary Science Conference, vol. 36, 2005, Abstr. No. 1985.
- [72] P. Vontobel, E. Lehmann, W.D. Carlson, Comparison of X-ray and neutron tomography investigations of geological materials, *IEEE Trans. Nucl. Sci.* 52 (2005) 338–341.
- [73] B. Winkler, K. Knorr, A. Kahle, P. Vontobel, E. Lehmann, B. Hennion, G. Bayon, Neutron imaging and neutron tomography as non-destructive tools to study bulk-rock samples, *Eur. J. Mineral.* 14 (2002) 349–354.
- [74] B. Masschaele, M. Dierick, L. Van Hoorebeke, V. Cnudde, P. Jacobs, The use of neutrons and monochromatic X-rays for non-destructive testing in geological materials, *Environ. Geol.* 46 (2004) 486–492.
- [75] M. Solymar, E. Lehmann, P. Vontobel, A. Nordlund, Relating variations in water saturation of a sandstone sample to pore geometry by neutron tomography and image analysis of thin sections, *Bull. Eng. Geol. Environ.* 62 (2003) 85–88.
- [76] I.F. Lunati, P. Vontobel, W. Kinzelbach, E. Lehmann, Laboratory visualization of two-phase flow in a natural fracture by neutron tomography, *Proceedings: Groundwater in Fractured Rocks*, Prague, Czech Republic, 2003.
- [77] R.T. Lopes, A.P. Bessa, D. Braz, E.F.O. de Jesus, Neutron computerized tomography in compacted soil, *Appl. Radiat. Isotopes* 50 (1999) 451–458.
- [78] J.W. Bishop, N.J. Huerta, N.J. Beukes, D.Y. Sumner, Neutron computed tomography and description of molar tooth structures in the Neoproterozoic Boomplaas and Monteville Formations, and the Paleoproterozoic Hotazel Iron-Formation, South Africa, *Geol. Soc. Am. Abstr. Prog.* 36 (2004) 251.
- [79] N. Nestle, T. Baumann, R. Neissner, Magnetic resonance imaging in environmental science, *Environ. Sci. Technol.* 36 (2002) 154A–160A.
- [80] P.T. Callaghan, *Principles of Magnetic Resonance Microscopy*, Clarendon Press, Oxford, 1991, 492 pp.
- [81] T. Steiger, Nuclear magnetic resonance imaging in paleontology, *Comput. Geosci.* 27 (2001) 493–495.
- [82] M.K. Gingras, B. MacMillan, B.J. Balcom, Visualizing the internal physical characteristics of carbonate sediments with magnetic resonance imaging and petrography, *Bull. Can. Pet. Geol.* 50 (2002) 363–369.
- [83] M.K. Gingras, B. MacMillan, B.J. Balcom, T. Saunders, S.G. Pemberton, Using magnetic resonance imaging and petrographic techniques to understand the textural attributes and porosity distribution in *Macaronichnus*-burrowed sandstone, *J. Sediment. Res.* 72 (2002) 552–558.

- [84] S.M. Belliveau, T.L. Henselwood, C.H. Langford, Soil wetting processes studied by magnetic resonance imaging: correlated study of contaminant uptake, *Environ. Sci. Technol.* 34 (2000) 2439–2445.
- [85] K.-H. Herrmann, A. Pohlmeier, D. Gembris, H. Vereecken, Three-dimensional imaging of pore water diffusion and motion in porous media by nuclear magnetic resonance imaging, *J. Hydrol.* 267 (2002) 244–257.
- [86] S. Ostwald, W. Kinzelbach, A. Greiner, G. Brix, Observation of flow and transport processes in artificial porous media via magnetic resonance imaging in three dimensions, *Geoderma* 80 (1997) 417–429.
- [87] S. Baraka-Lokmane, G. Teutsch, I.G. Main, Influence of open and sealed fractures on fluid flow and water saturation in sandstone cores using magnetic resonance imaging, *Geophys. J. Int.* 147 (2001) 263–271.
- [88] M.W. Becker, M. Pelc, R.V. Mazurchuk, J. Sperryak, Magnetic resonance imaging of dense and light non-aqueous phase liquid in a rock fracture, *Geophys. Res. Lett.* 30 (2003) 1646, doi:10.1029/12003GL017375.
- [89] D.M. Mueth, G.F. Debregeas, G.S. Karczmar, P.J. Eng, S.R. Nagel, H.M. Jaeger, Signatures of granular microstructure in dense shear flows, *Nature* 406 (2000) 385–389.
- [90] H. Eicken, C. Bock, R. Wittig, H. Miller, H.-O. Poertner, Magnetic resonance imaging of sea-ice pore fluids: methods and thermal evolution of pore microstructure, *Cold Reg. Sci. Technol.* 31 (2000) 207–225.
- [91] C. Bock, H. Eicken, A magnetic resonance study of temperature-dependent microstructural evolution and self-diffusion of water in Arctic first-year sea ice, *Ann. Glaciol.* 40 (2005) 189–190.
- [92] S. Kasperl, P. Vontobel, Application of an iterative artefact reduction method to neutron tomography, *Nucl. Instrum. Methods Phys. Res., Sect. A, Accel. Spectrom. Detect. Assoc. Equip.* 542 (2005) 392–398.
- [93] B. Masschaele, S. Baechler, P. Cauwels, M. Dierick, J. Jolie, W. Mondelaers, First results of micro-neutron tomography by use of a focusing neutron lens, *Rad. Phys. Chem.* 61 (2001) 623–624.
- [94] S. Baechler, N. Kardjilov, M. Dierick, J. Jolie, G. Kühne, E. Lehmann, A. Materna, New features in cold neutron radiography and tomography. Part I: thinner scintillators and a neutron velocity selector to improve the spatial resolution, *Nucl. Instrum. Methods Phys. Res., Sect. A, Accel. Spectrom. Detect. Assoc. Equip.* 491 (2002) 481–491.
- [95] N. Kardjilov, S. Baechler, M. Bastürk, M. Dierick, J. Jolie, E. Lehmann, T. Materna, B. Schillinger, P. Vontobel, New features in cold neutron radiography and tomography: Part II. applied energy-selective neutron radiography and tomography, *Nucl. Instrum. Methods Phys. Res., Sect. A, Accel. Spectrom. Detect. Assoc. Equip.* 501 (2003) 536–546.
- [96] G.C. Tyrell, Phosphors and scintillators in radiation imaging detectors, *Nucl. Instrum. Methods Phys. Res., Sect. A, Accel. Spectrom. Detect. Assoc. Equip.* 546 (2005) 180–187.



William D. Carlson is professor of geology and director of UTCT, the high-resolution X-ray computed tomography facility at the University of Texas at Austin. His current research is focused on identifying crystallization mechanisms and quantifying reaction kinetics in metamorphic rocks, to understand rates of equilibration and scales of disequilibrium in the deep crust. His efforts at UTCT are aimed at providing the earth and planetary sciences community with ready access to state-of-the-art high-resolution XCT technology. He was the recipient of the 2005 Dana Medal of the Mineralogical Society of America.